Impact of carrier injector design on the threshold of interband cascade lasers

Takuma Sato (佐藤拓磨),^{1,2} Borislav Petrović,³ Robert Weih,⁴ Fabian Hartmann,³ Sven Höfling,³ Stefan Birner,¹ Christian Jirauschek,² and Thomas Grange⁵

¹⁾ nextnano GmbH, Konrad-Zuse-Platz 8, 81829 Munich, Germany

(*Electronic mail: takuma.sato@nextnano.com)

(Dated: 21 November 2025)

We investigate theoretically how the injector region design of interband cascade lasers (ICLs) impacts the threshold carrier and current densities. The model combines a polarization-sensitive 8-band $\mathbf{k} \cdot \mathbf{p}$ calculation, electrostatics, and a microscopic calculation of Auger recombination rates. The carrier-carrier scattering is included to lowest order within the non-equilibrium Green's function formalism. It captures the combined effects of charge carrier redistribution, parasitic absorption and bias voltage on the Auger recombination rate. We show that heavily doping the electron injector suppresses the dominant multi-hole Auger recombination by reducing the hole population of the recombination quantum wells. This agrees with the experimental observation that the heavy doping reduces threshold currents. Yet, our model suggests that the Auger recombination alone is not sufficient to explain the increase of threshold currents at high doping concentrations. Furthermore, by introducing indium to the conventional GaSb hole injector wells, we explain the rule of thumb from experiments that raising the hole injector levels does not outperform the doping strategy. Our model provides physical insights toward optimization of ICL carrier injectors.

I. INTRODUCTION

Gas sensing application of interband cascade lasers (ICLs) as a mid-infrared source has demanded continuous improvement of their design¹ since the first experimental realization by Yang in 1997.² The ICLs realized to this date consume less input power than quantum well (QW) and quantum cascade lasers, operating above room temperature. ICLs are therefore ideal for portable devices for environmental monitoring,³ industrial process control,⁴ clinical breath analysis,⁵ and telecommunications.⁶

Theoretical analysis has played a central role in the design of ICL active regions. In the dawn of the development. Mever et al. proposed the "W-shaped" quantum wells (W-QWs) for radiative recombination in midinfrared interband lasers, demonstrating with an 8-band $\mathbf{k} \cdot \mathbf{p}$ calculation that the type-II QWs improve the electrical confinement and suppress Auger recombination compared to type-I band alignments. The recombination QWs have been subsequently optimized at various emission wavelengths to enhance their oscillator strength $^{8-13}$ and to reduce parasitic intra-valence absorptions. $^{\hat{1}3-15}$ A correlation has been observed between calculated parasitic absorption and measured threshold current densities. Recombination QWs may further be optimized in terms of Auger suppression; for InAs-based type-II superlattices, Grein et al. 16,17 proposed to engineer the miniband dispersion by strain.

While theoretical predictions about ICLs have mainly

focused on the recombination QWs, injector engineering has been experimentally proven to be effective for reducing threshold current densities; Vurgaftman et al. 18,19 achieved 134 A/cm² by heavily n-doping the electron injector wells. Experiments 18,20 indicate an optimal doping concentration of $5\times10^{18}~\mathrm{cm}^{-3}$. While Vurgaftman et al. attributed it to a rebalancing of the electron and hole concentrations in the recombination region, the connection between carrier balance and Auger rates remains unclear due to the limitations of phenomenological models. Despite successive experimental refinements in the injector design, 21,22 a comprehensive understanding is still lacking as to how and why the injector design affects the threshold current. 1 Answering these questions requires a microscopic calculation of Auger recombination.

In this paper, we systematically calculate how the injector design impacts threshold carrier and current densities. The threshold is found through a bias-dependent 8-band $\mathbf{k} \cdot \mathbf{p}$ gain calculation considering the entire ICL period and parasitic intraband absorptions (subsection IIB). Without relying on the phenomenological Auger coefficients, we calculate Auger recombination rates from the GW self-energy (subsection IIC). Sec. III discusses the correlation of the injector designs with the carrier balance and threshold current density. Sec. IV concludes the analysis and outlines future perspectives.

²⁾ TUM School of Computation, Information and Technology, Technical University of Munich, Hans-Piloty-Straße 1, 85748 Garching, Germany

³⁾ Julius-Maximilians-Universität Würzburg, Physikalisches Institut, Lehrstuhl für Technische Physik, Am Hubland, 97074 Würzburg, Germany

⁴⁾nanoplus Advanced Photonics Gerbrunn GmbH, Oberer Kirschberg 4, 97218 Gerbrunn, Germany

⁵⁾ nextnano Lab, 12 chemin des prunelles, 38700 Corenc, France

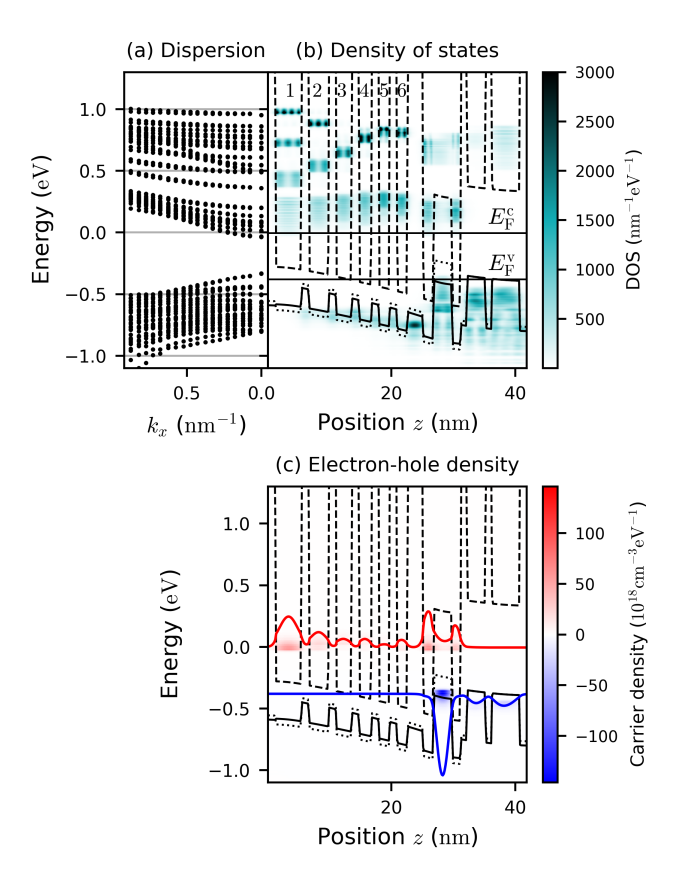


FIG. 1. One active region period of the reference ICL in Table I at the potential drop per period of 375 meV. (a) In-plane dispersion in the entire reciprocal space included in the simulations. (b) Density of states integrated over the in-plane momentum. The horizontal lines indicate the quasi Fermi levels. The dashed, dotted, and solid curves represent the conduction, heavy-hole, and light-hole bandedges of the bulk materials, respectively. (c) Energy-resolved electron and hole densities in quasi-equilibrium (colormap). Red and blue curves show the relative magnitude of the energy-integrated electron and hole densities, respectively.

II. METHOD

A. Active region design

We take the ICL structures of Vurgaftman et al.¹⁸ as an example. The ICLs emit photons of wavelengths from 3.6 µm to 3.9 µm and its electron injector consists of 6 quantum wells (Fig. 1). We vary the injector designs as listed in Table I. The threshold current densities of the reference and some of the 2- and 4-well doping designs were measured experimentally. The doping series can be compared on an equal footing by the sheet doping density in one period $N_{\rm D}$ (cm⁻²). The z axis is set along the growth direction.

TABLE I. Doping profile of the electron injector (in $10^{18}~{\rm cm}^{-3}$) and QW material for the hole injector among the design variations in this study. y is the doping concentration within each electron injector QW. The value for the indium series has been chosen to maintain the same sheet doping density as the reference.

	Electron injector doping				Hole injector		
Design	1	2	3	4	5	6	
Reference	0.4	0.4	0.4	0.4	0	0	GaSb
2-well	0	0	0	y	y	0	GaSb
4-well	0	y	y	y	y	0	GaSb
Indium	0	0.506	0.506	0.506	0.506	0	$Ga_{1-x}In_xSb$

B. Carrier distribution and gain

To model the intricacy of threshold carrier densities, i.e., the interplay of band coupling, electrostatics, and parasitic absorptions, we conduct the simulations sketched in Fig. 2. The key features are that (i) the carrier distribution in an entire cascade period is solved selfconsistently with Poisson's equation, (ii) material gain and parasitic absorption are calculated in the active region, (iii) the lasing thresholds are found considering the optical losses outside of the cascade structure. Since we focus our analysis on the lasing threshold, we may neglect stimulated emission. In this regime, interband transitions are much slower than the electron-hole generation at the semimetallic interface and relaxation between the injectors and W-QW. Indeed, measured threshold cur- $\mathrm{rents}^{18,20,23}$ and carrier densities calculated below translate to the upper laser state lifetimes ranging from 0.5 ns to 1 ns, which is much longer than the gain recovery time of a few picoseconds measured for 3.3 µm ICLs. 24 This justifies assuming constant Fermi levels for the electrons and holes, which are energetically split by the potential drop per period (quasi-equilibrium approximation, ²⁵ see Fig. 1). As the carrier relaxation to the lattice temperature is on the picosecond timescale, the carrier temperature $T_{\rm e}$ in the Fermi–Dirac functions can be set to the lattice temperature $T_{\rm L} = 300$ K.

To calculate the carrier distribution and gain. we have extended the quantum transport simulator $nextnano.NEGF^{26}$ based on the non-equilibrium Green's functions (NEGF) formalism, to interband devices. The 2-band models, implemented into interband NEGF transport solvers in previous works, ^{27,28} are not sufficient for capturing the parasitic absorption in the valence band of ICLs. Thus, we have implemented the 8-band $\mathbf{k} \cdot \mathbf{p}$ Hamiltonian and material parameters described in Appendix A. At the beginning of a simulation, energy eigenstates and subband dispersions of given heterostructure are found without bias voltage at tens of in-plane wavevectors. The in-plane anisotropy of the band structure²⁹ is not expected to affect the subband occupation significantly in the quasi-equilibrium limit and is therefore neglected. Second, we select conduction (valence) subbands

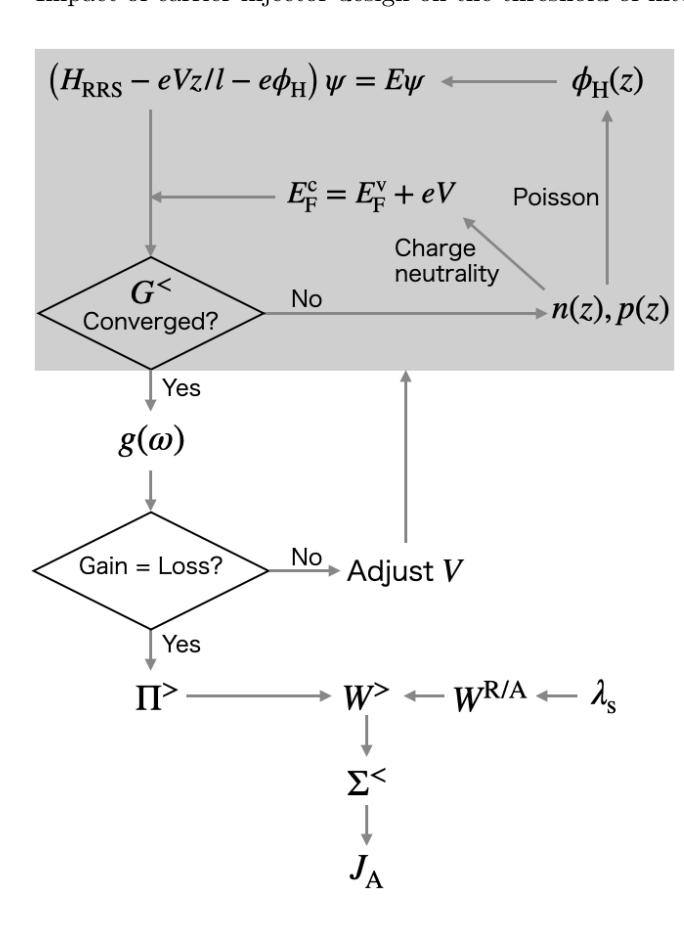


FIG. 2. Simulation flow for calculating the threshold carrier densities and Auger recombination current. V and l are the potential drop per period and period length, respectively. The other quantities are defined in the main text.

by the energy range of $E^{\rm c}_{\rm cutoff}$ ($E^{\rm v}_{\rm cutoff}$) from their respective ground states and discard other subbands. The in-plane wavevector is considered up to the point where the lowest conduction subband rises by $E_{\text{cutoff}}^{\parallel}$. The actual cut-off energies used in the simulations are summarized in Appendix B. Fig. 1 shows the in-plane dispersion and density of states of the selected subbands, confirming that these energies cover the range relevant for the optical transitions and the Auger recombination described in Sec. II C. In this subspace, the position operator \hat{z} is diagonalized to obtain localized modes, which we refer to as the reduced real space (RRS) basis functions.^{26,30} The Green's function of electrons and the Hamiltonian are represented as matrices G and H_{RRS} in this basis, respectively. Our Green's functions are in the "electron picture" and thus do not rely on the concept of holes; selected conduction and valence subbands are first emptied entirely, and the lesser Green's function $G^{<}$ describes the state occupation by electrons, regardless of whether the energy is above or below the band gap. Third, the quasi-Fermi levels $E_{\rm F}^{\rm c/v}$ for the conduction and valence bands and the Hartree potential $\phi_{\rm H}$ are sought to simultaneously satisfy the charge neutrality and Poisson's equation

(Fig. 2). The elastic scattering due to crystal imperfections is replaced by a phenomenological line broadening γ_{subband} .

Finally, once the Green's functions have converged, we extract level populations and calculate the optical gain spectrum under the dipole approximation using Fermi's golden rule,³¹

$$g(\hat{e}, \omega) = \frac{\pi e^2}{\hbar c \epsilon_0 \sqrt{\epsilon(\omega)}} \frac{1}{V} \sum_{n > m} \sum_{\mathbf{k}_{\parallel}} \times O_{nm}(\hat{e}, \mathbf{k}_{\parallel}) \left[P_n(\mathbf{k}_{\parallel}) - P_m(\mathbf{k}_{\parallel}) \right] \times \mathcal{L}(E_n(\mathbf{k}_{\parallel}) - E_m(\mathbf{k}_{\parallel}) - \hbar \omega), \tag{1}$$

where $e \ (> 0)$, c, ϵ_0 , $\epsilon(\omega)$, and $\mathbf{k}_{\parallel} = (k_x, k_y)$ are the elementary charge, speed of light, vacuum permittivity, (spatially-averaged) dielectric function, and in-plane wavevector, respectively. The indices m and n enumerate the initial and final subbands. As the summation includes all subbands in Fig. 1, Eq. (1) contains interband, intra-conduction, and intra-valence transitions. The oscillator strengths O_{nm} are calculated from the light polarization vector \hat{e} and the 8-band momentum operator $\hat{p}_j(\mathbf{k}_{\parallel})$ as described in Appendix C. $E_n(\mathbf{k}_{\parallel})$ are the eigenvalues of $\mathbf{H}_{\rm RRS}$ plus bias. The subband populations P_n are calculated from the converged lesser Green's functions transformed to the energy eigenbasis,

$$P_n(\mathbf{k}_{\parallel}) = -i \int \frac{\mathrm{d}E}{2\pi} G_{nn}^{<}(\mathbf{k}_{\parallel}, E).$$
 (2)

The energy broadening is taken to be a Gaussian

$$\mathcal{L}(E) = \frac{1}{\sqrt{2\pi}\gamma_{\text{gain}}} \exp\left(-\frac{E^2}{2\gamma_{\text{gain}}^2}\right).$$
 (3)

For simplicity, we use a fixed linewidth $\gamma_{\rm gain}$ for all transitions. Indeed, the shape of the gain peak is predominantly determined by the in-plane dispersion. Lasing starts when the modal gain maximum matches the sum of the mirror and cladding losses,

$$\Gamma g_{\rm th} = \frac{1}{L} \ln \left(\frac{1}{R} \right) + (1 - \Gamma) \alpha_{\rm clad},$$
 (4)

where $L_{\rm cav}$, R, Γ , and $\alpha_{\rm clad}$ are the cavity length, mirror reflectivity, confinement factor of the optical mode in the active region, and cladding loss, respectively. Eq. (4) determines the threshold voltage $V_{\rm th}$.

We analyze the threshold carrier balance in the W-QW by the average densities (cm^{-3}) ,

$$\bar{n}_{\rm th}^{\rm w} \equiv \frac{1}{w_{\rm e}} \int_{\rm WOW} n_{\rm th}(z) \, \mathrm{d}z,$$
 (5a)

$$\bar{p}_{\rm th}^{\rm w} \equiv \frac{1}{w_{\rm h}} \int_{\rm WOW} p_{\rm th}(z) \, \mathrm{d}z,$$
 (5b)

where the spatial extent of the upper (lower) laser states, $w_{\rm e(h)} = \int_{\rm WOW} |\psi_{\rm e(h)}(z)|^2 \, {\rm d}z/|\psi_{\rm e(h)}|_{\rm max}^2 =$

2.96 (2.11) nm, remain approximately constant in this study as we do not modify the W-QW. Not normalizing by $w_{e(h)}$, i.e., comparing the electron and hole sheet densities, would miss the significant difference in spatial confinement of the electrons and holes.

C. Auger recombination rates

Since the Auger mechanism dominates the non-radiative recombination of ICLs at room temperature, we assess different injector designs in terms of Auger rates. The rates are usually modelled phenomenologically and read in the non-degenerate (Maxwell–Boltzmann) limit 32,33

$$R_{\mathcal{A}} = C_{\mathcal{D}} n^2 p + C_{\mathcal{D}} p^2 n, \tag{6}$$

where $C_{\rm n/p}$ characterize the strength of the eeh and ehh Auger processes, respectively. The ratio $C_{\rm n}/C_{\rm p}$ would dictate how the carrier rebalancing reduces the threshold current, but has uncertainty due to the following reasons. First, $C_{\rm n/p}$ depend on temperature and device geometry as they reflect the availability of high-energy states for the "partner" carrier to be scattered into. Eq. (6) can be fitted to experiments, but cannot predict the Auger recombination in newly-designed QWs. As the eeh and ehh processes cannot be measured individually, the estimations of ICL Auger coefficients^{34,35} assumed equal volume densities of electrons and holes. While it is a good approximation for photodetectors and QW lasers, it obscures the relation between the carrier balance and Auger rates in ICLs. Second, Eq. (6) grows as a cubic function in carrier densities, but measurements show a deviation from it in the degenerate regime, in which the probability of finding the recombining electron-hole pair approaches unity. Experiments and calculations for midinfrared QW devices 36-38 confirm this; the density dependence reduces to quadratic or even less in the degenerate regime. This makes the fitting of Eq. (6) to experiments challenging. The non-degenerate approximation seems inappropriate for the present ICL structure, too. Fig. 1 shows that, at the lasing threshold, the ground states in the conduction and valence bands overlap with the quasi Fermi levels. As a result, Eq. (6) is limited in explaining the correlation between the carrier balance and Auger rates in ICLs.

Microscopically, the Auger process and its inverse process, impact ionization, are types of carrier-carrier scattering via Coulomb interaction. The interaction is short-range due to the screening by other carriers. Earlier works^{17,36,39-41} studied the scattering under the Born approximation. Calculation based on Fermi's golden rule does not rely on phenomenological parameters and is therefore predictive. The method has explained Auger rates in several QW designs¹⁷ and at low temperatures.⁴¹ Furthermore, Hader et al.^{37,38} solved the semiconductor Bloch equations, including the carrier-carrier scattering in the second Born–Markov approximation. The

calculated threshold currents of near-infrared QW lasers matched well with the measurements up to room temperature.

In view of future integration with quantum transport, we opt here for the NEGF formalism, in which carrier-carrier scattering can be included at different levels of sophistication. Since the Hartree–Fock approximation neglects the inelastic scattering and hence the Auger process, we use the next-order treatment of the Coulomb interaction described in Appendix D. Electrons are scattered into (out of) a state at energy E at the rate given by the lesser (greater) components, $\mathbf{\Sigma}^<(E)$ ($\mathbf{\Sigma}^>(E)$), of the GW self-energy. The Hartree potential is calculated from Poisson's equation and incorporated into the Hamiltonian (Fig. 2).

The net interband current is given by Auger rate minus impact ionization rate. In quasi-equilibrium, the ratio of the latter to former is $\exp\left[-(E_{\rm F}^{\rm c}-E_{\rm F}^{\rm v})/(k_{\rm B}T_{\rm e})\right]$, ¹⁶ where $k_{\rm B}$ and $T_{\rm e}$ are the Boltzmann constant and the carrier temperature, respectively. In mid-infrared ICLs at room temperature close to threshold, $E_{\rm F}^{\rm c}-E_{\rm F}^{\rm v}\gtrsim E_{\rm ph}\gg k_{\rm B}T_{\rm e}$, where $E_{\rm ph}$ is the photon energy, so that impact ionization is negligible. The interband current due to the Auger mechanism is then given by

$$J_{\rm A} = \frac{e}{\hbar} \int \frac{\mathrm{d}\mathbf{k}_{\parallel}}{(2\pi)^2} \int_{\rm VB} \frac{\mathrm{d}E}{2\pi} \mathrm{Tr} \left[\mathbf{\Sigma}^{<}(\mathbf{k}_{\parallel}, E) \mathbf{G}^{>}(\mathbf{k}_{\parallel}, E) \right],$$
(7)

where $G^{>}$ is the greater Green's function of electrons. The energy integration is performed below the heterostructure band gap. In steady states, the lesser component of the GW self-energy is represented in the RRS basis as (see Appendix D)

$$\Sigma_{z_1 z_2}^{<}(\mathbf{k}_{\parallel}, t) = i \int \frac{\mathrm{d}\mathbf{q}_{\parallel}}{(2\pi)^2} G_{z_1 z_2}^{<}(\mathbf{k}_{\parallel} + \mathbf{q}_{\parallel}, t) \times \left[W_{z_1 z_2}^{c<}(\mathbf{q}_{\parallel}, t) + W_{z_1 z_2}^{c<}(\mathbf{q}_{\parallel}, t) \right], \quad (8)$$

where ${m W}^{{
m c/v}<}(t)={m W}^{{
m c/v}>}(-t)$ are the Fourier-transforms of

$$W_{z_{1}z_{2}}^{c/v>}(\mathbf{q}_{\parallel}, E') = \sum_{z_{3}z_{4}} W_{z_{1}z_{3}}^{R}(\mathbf{q}_{\parallel}, E') \Pi_{z_{3}z_{4}}^{c/v>}(\mathbf{q}_{\parallel}, E') W_{z_{4}z_{2}}^{A}(\mathbf{q}_{\parallel}, E').$$
(9)

We distinguish Π^c and Π^v by the range of the energy integration; they describe the intra-conduction and intravalence band transitions, respectively, of the "partner" electron. The first and second terms in Eq. (8) therefore correspond to the eeh and ehh Auger processes, respectively. The retarded and advanced screened Coulomb potentials between two particles at positions z_1 and z_2 are (Appendix D)

$$W_{z_1 z_2}^{\text{R/A}}(\mathbf{q}_{\parallel}) \approx \frac{e^2}{2\epsilon_0 \epsilon(0) L^2} \frac{e^{-q_{\text{s}}|z_1 - z_2|}}{q_{\text{s}}},$$
 (10)

where $\epsilon(0)$ is the static dielectric constant averaged over one period, L^2 the normalization area, and $q_s = \sqrt{\lambda_s^{-2} + q_\parallel^2}$. A screening length λ_s of 4 nm is assumed to be reasonable based on the plasma screening models of Fermi gases (see Appendix D). Since $\mathbf{W}^{\mathrm{R/A}}(\mathbf{q}_\parallel)$ decays exponentially in the reciprocal space, the \mathbf{q}_\parallel -dependence of $\mathbf{\Pi}^>$ in Eq. (9) is irrelevant. We therefore approximate the polarization function by its $q_\parallel = 0$ value. The scattered (hot) electrons in the excited subbands are expected to have short coherence lengths due to other scattering mechanisms not considered here. As the RRS modes are well-confined in each well, we only consider the diagonal terms of the polarization functions,

$$\Pi_{z_{1}z_{1}}^{c>}(0, E') = -i \int \frac{d\mathbf{q}'_{\parallel}}{(2\pi)^{2}} \int_{E_{b}}^{\infty} \frac{dE''}{2\pi} \times G_{z_{1}z_{1}}^{>}(q'_{\parallel}, E' + E'') G_{z_{1}z_{1}}^{<}(q'_{\parallel}, E''), (11)$$

$$\Pi_{z_{1}z_{1}}^{v>}(0, E') = -i \int \frac{d\mathbf{q}'_{\parallel}}{(2\pi)^{2}} \int_{-\infty}^{E_{b}-E'} \frac{dE''}{2\pi} \times G_{z_{1}z_{1}}^{>}(q'_{\parallel}, E' + E'') G_{z_{1}z_{1}}^{<}(q'_{\parallel}, E''), (12)$$

where $E_{\rm b}$ is the energy border located within the heterostructure band gap. As long as the Auger recombination is slower than the intraband transport, i.e., quasi-equilibrium approximation is valid, the GW self-energy needs to be evaluated just once after the charge distribution and Hartree potential have converged (Fig. 2).

In the following, we assess by Eq. (7) how the injector design affects the carrier balance and threshold current.

III. RESULTS AND DISCUSSION

We first investigate the gain spectra. Fig. 3(a) illustrates the contribution of the interband and intraband transitions to the gain spectrum of the 4-well doping design with $y = 5 \times 10^{18} \text{ cm}^{-3}$. The gain peak occurs at the wavelength 3.73 µm, which is within the range of the measurement. 18 In general, the interband gain is reduced by both intra-conduction and intra-valence absorptions because the $\mathbf{k} \cdot \mathbf{p}$ coupling blurs the selection rules. In addition, an oblique light polarization activates both optical transitions. Although ICL laser levels barely couple to TM-polarized light, the polarization component of the lasing-mode along the growth may not be negligible. 42 Fig. 3(b) depicts the polarization angle dependence of the parasitic absorptions at the peak photon energy of the net gain spectra. It shows that the out-of-plane polarization component appreciably increases the intraconduction absorption even at small oblique angles. In the absence of concrete data about light polarization in ICLs, we choose a slightly oblique angle of 3.4° .

Fig. 4 compares various properties of the designs in Table I. Figs. 4(a1–a2) show that the electron densities in the W-QW and the electron injector increase approximately linearly with the sheet doping density. Heavily

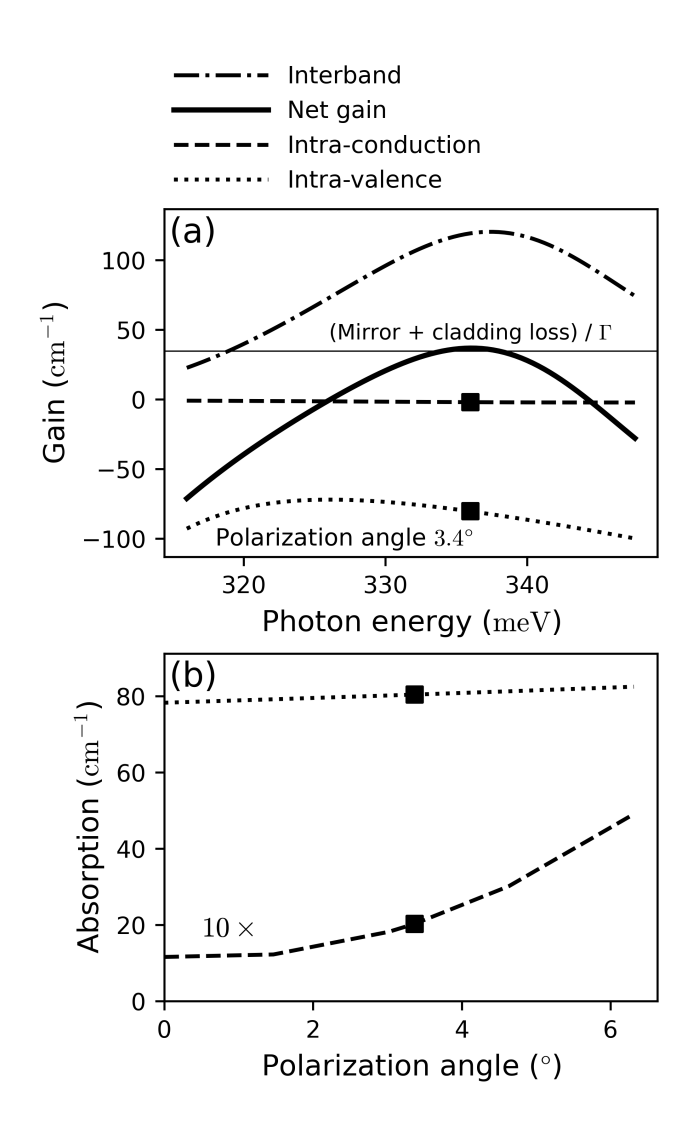


FIG. 3. Optical spectra of the reference design in Table I at the threshold voltage $V_{\rm th}=375~{\rm mV}.$ (a) Net gain spectrum and its decomposition into the interband, intra-conduction and intra-valence contributions. Black line indicates the losses outside of the active region. (b) Intraband absorption coefficients at maximum gain as a function of the polarization angle with respect to the x-y plane. In both panels, squares mark the values extracted for the analysis of the parasitic absorption.

doping the electron injector raises both quasi-Fermi levels and thereby decreases the hole concentration in the W-QW. Our model thus reproduces the carrier rebalancing in W-QWs. Figs. 4(b1-b2) track the parasitic absorptions at the gain peak, that is, the squares in Figs. 3, showing that (i) the absorption is much stronger in the valence band due to the light polarization almost perpendicular to the growth direction, and that (ii) the intravalence absorption decreases following the trend of the hole concentration in Figs. 4(a1-a2). For given sheet doping density, the 4-well doping reduces the band bending of the electron injector and populates the widest (i.e.,

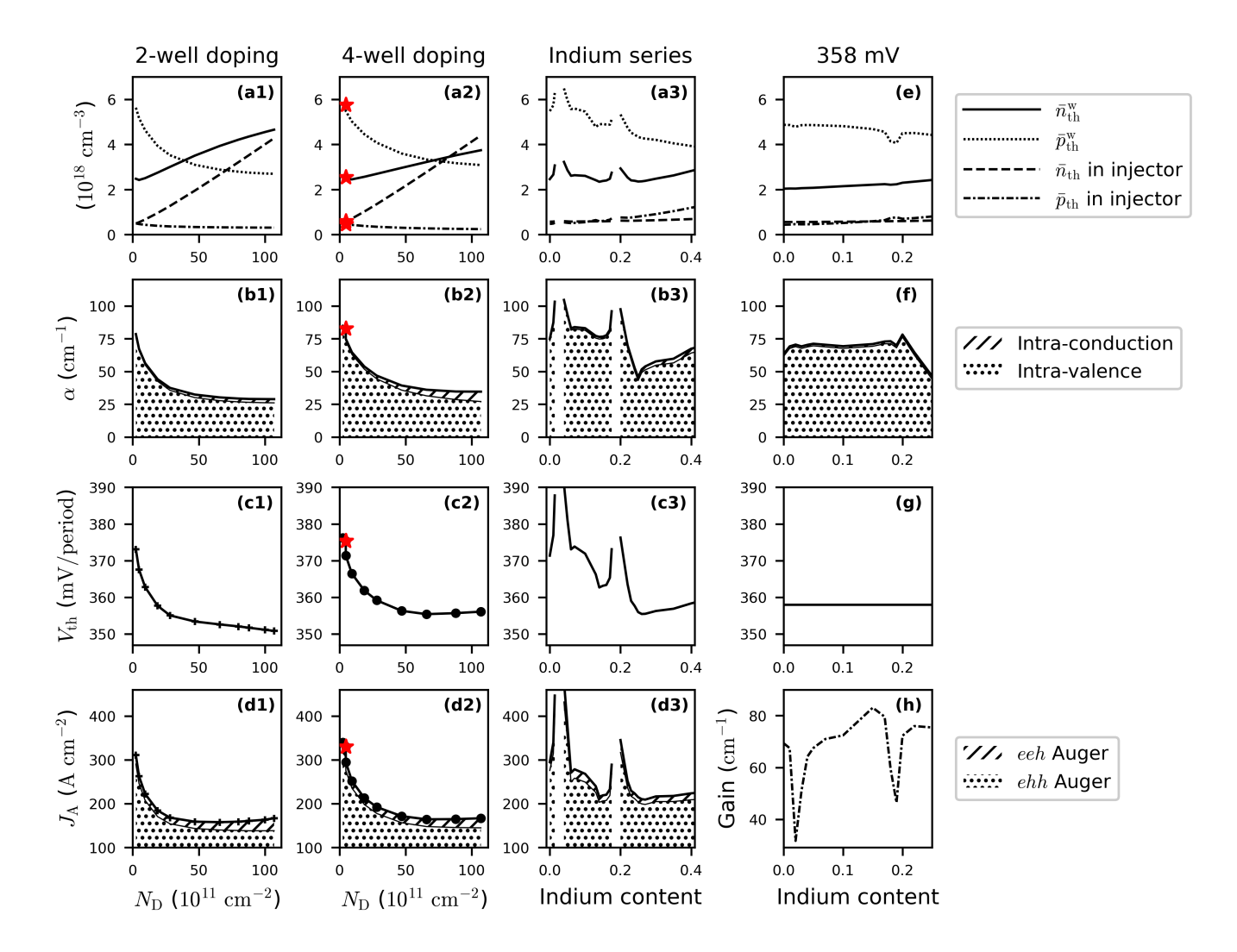


FIG. 4. Impact of the injector design variations on ICL performance figures. Red stars indicate the reference structure in Table I. (a) Threshold carrier densities in the W-QW and injectors in the doping and indium series. The W-QW carrier densities are defined by Eqs. (5), whereas the injector counterparts are simply averaged by the injector lengths. (b) Optical absorption coefficients at the photon energies of maximum gain and their breakdown to the intra-conduction and intra-valence contributions. (c) Potential drop per period at the lasing thresholds. (d) Interband currents due to the *eeh* and *ehh* Auger mechanisms. (e–g) Corresponding data from the indium series at a fixed bias of 358 mV. (h) Peak values of the interband gain without parasitic absorptions.

first) QW more, thereby increasing the intra-conduction absorption compared to the 2-well doping. Nevertheless, it remains a minor contribution to the total parasitic absorption in the active region. The heavy doping of the electron injector therefore improves carrier balance and reduces the intra-valence absorption, with the effect being mostly insensitive to which electron injector wells are doped. The decreasing absorption in Figs. 4(b1-b2) reduces the threshold voltage, shown in Figs. 4(c1-c2), by 5% to 6%. The trend stagnates at higher doping densities. Figs. 4(d1-d2) depict the interband currents calculated by Eq. (7). The eeh process is significantly slower than the ehh one even at the perfect carrier balance in Figs. 4(a1-a2). In the phenomenological model [Eq. (6)], this would mean that $C_p > C_n$, but the valid-

ity of the model is questionable in the degenerate regime (see Sec. II C). The eeh process is much slower because the subbands are more sparse in the conduction than in the valence band (Π^c is smaller than Π^v). While the eeh contribution increases with doping, the ehh rate drops more significantly due to the decreasing hole concentration in the W-QW, resulting in an overall reduction of the Auger current. Our results show that reducing the hole population in the W-QW is effective for minimizing threshold currents owing to the selection rules and high density of states in the valence band.

The relative contribution of the eeh mechanism to the total Auger current is larger in the 2-well than in the 4-well doping series in Figs. 4(d1–d2) because the carrier rebalancing in the W-QW occurs at lower doping levels

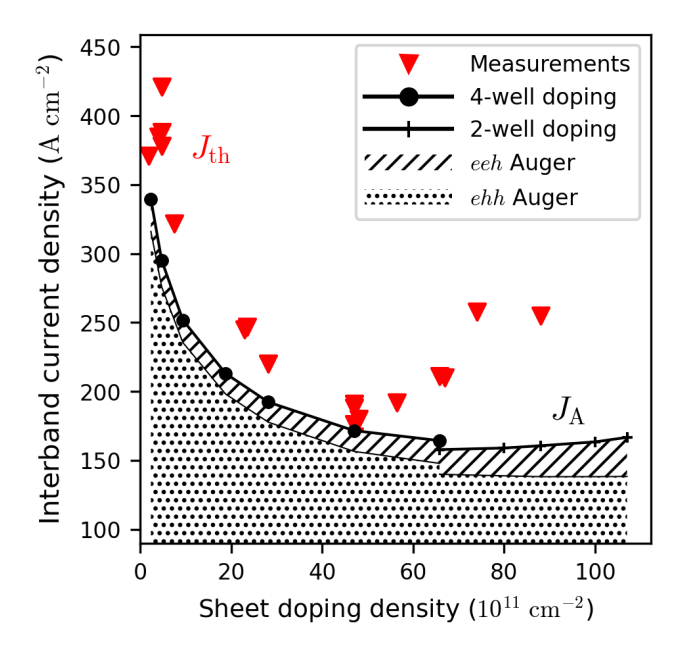


FIG. 5. Threshold current densities from the measurements ^{18,20,23} (triangles) and Auger currents from the simulations (curves) against sheet doping density.

in Fig. 4(a1).

The strategy above was to reduce the hole population in the W-QW indirectly by doping the electron injector. We note in Figs. 4(a1-a2) and (d1-d2) that most of the holes reside in the W-QW and contribute to the ehh Auger process. This motivates another strategy: distribute more holes to the injector. However, experimental observations discourage raising the subbands in the two hole injector QWs closer to or higher than the topmost hole state in the W-QW.¹ To elucidate the reason for this empirical rule of thumb, we introduce indium to the hole injector QWs (see Table I). Experimentally, the indium content in such material combination is commonly kept not exceeding 40% to avoid high strain and defects. The hole injector levels rise by 85 meV to 90 meV when the indium content is increased from 0% to 40%. As the threshold was not reached at 3% and 19%, corresponding data are omitted in Figs. 4(a3–d3).

Fig. 4(a3) shows the threshold carrier densities in the indium series and confirms the carrier rebalancing in the W-QW, but the effect is weaker than the electron injector doping. In contrast to Figs. 4(a1–a2), the indium series barely increases the electron population in the first electron injector QW, which suppresses the intra-conduction absorption in Fig. 4(b3). The benefit is smaller, however, than the cost of the higher hole concentration in the hole injector, which enhances the parasitic intra-valence absorption.

The sharp spikes in Fig. 4(c3) can be understood from the behavior at a fixed bias voltage of 358 mV plotted in Figs. 4(e-h). Fig. 4(h) tracks the maximum interband gain in Fig. 3. By studying the wavefunctions, we at-

tribute the two dips to a hybridization of the hole states in the W-QW and hole injector. As the spikes in Fig. 4(f) are much less significant, the hybridization seems to be the major reason for the spikes in Fig. 4(c3). A higher voltage increases the population inversion, but also enhances the parasitic absorptions in Fig. 4(b3), preventing the laser from reaching the threshold.

The threshold voltage appears compelling at the indium content of 25% to 40% compared with the doping series. However, Figs. 4(a3) and (d3) show that a higher hole density in the W-QW increases the ehh Auger recombination. This underlines again the importance of reducing the hole concentration for minimizing threshold currents. To summarize, the carrier rebalancing strategy by means of raising the hole injector levels fails to efficiently reduce the hole concentration in the recombination QWs and suffers from a stronger Auger recombination.

Fig. 5 compares the Auger recombination currents calculated by Eq. (7) with the measurements. 18,20,23 As the ehh process is dominant, reducing the hole population in the W-QW significantly decreases the threshold current in the left half of the plot. While the measured threshold currents increase in the right half, our simulation predicts a more flat trend. The choice of λ_s shifts the curve up- or downward, but does not alter its shape. At high doping, one might expect an enhanced parasitic absorption and hence a higher threshold voltage. However, the absorption is hindered by the selection rules of the conduction subbands for nearly TE-polarized light, as demonstrated in Figs. 4(b1-b2). Our model thus suggests that the Auger process alone is not sufficient to explain the increase of threshold currents at high doping concentrations. Radiative recombination does not explain it since our calculation (not shown) indicates that the spontaneous emission generates interband currents of merely 6 A cm⁻² to 9 A cm⁻². We do not expect a significant contribution from Shockley-Read-Hall recombination either since 3 µm to 5 µm ICLs with type-II recombination QWs are known to be tolerant to dislocations. 43,44 One possible reason is intrasubband absorptions mediated by scattering with lattice vibrations and imperfections. 45 This mechanism may increase the parasitic absorption particularly in the conduction band and raise the threshold voltage, 46 which increases the threshold carrier densities and hence the Auger rate. Another possible reason is the injection efficiency less than one. Experiments with ICLs grown on InAs or GaSb substrates imply that about 10% to 40% of the injected carriers either leak through sidewalls, or enter the laser levels but escape without recombination.^{1,47} The latter mechanism may be activated at lasing thresholds by the Auger process; the carrier-carrier scattering promotes the excess carriers in the W-QW to higher subbands, helping them overcome the barriers and travel to the next period without recombination [see Fig. 1(b)].

IV. CONCLUSION AND OUTLOOK

We have studied the impact of ICL injector designs on threshold current density by calculating the threshold carrier densities and Auger recombination rates. The model combines electrostatic effects, interband coupling, and in-plane momentum- and polarization-dependent gain calculation with a microscopic calculation of the Auger rates. Our conclusion is threefold. First, heavily doping the electron injector^{18,20} was shown to reduce the threshold current density essentially because the decrease of the hole concentration suppresses the dominant parasitic absorption and ehh-Auger process. Second, the Auger mechanism alone does not explain the increase of threshold currents at high doping densities. Other recombination mechanisms may need to be considered. Third, an alternative carrier rebalancing approach—raising the hole levels in the injector by $Ga_{1-x}In_xSb$ QWs—does not outperform the doping strategy. The indium series is less efficient in transferring holes from the W-QW to the hole injector, thereby suffering from a larger intra-valence absorption at this emission wavelength. This necessitates a larger population inversion, resulting in faster Auger recombination. Thus, our 8-band $\mathbf{k} \cdot \mathbf{p}$ NEGF modeling of ICLs provides physical insights to the impact of carrier injector designs on lasing thresholds.

Throughout this study, we kept the layer thicknesses and number of wells of the injectors constant to focus on the effect of the doping profile and well depth. When these parameters are optimized accordingly for each target emission wavelength, Auger rates may be reduced further. Our model offers a basis for future non-equilibrium quantum transport simulations beyond the quasi-equilibrium approximation used here. This may reveal insights into remaining questions such as (i) the limit of the quasi-equilibrium approximation, and (ii) mechanism and design-dependence of the escape of injected carriers from the recombination QW.

ACKNOWLEDGMENTS

We thank European Union's Horizon 2020 research and innovation program under the Marie Skłodowska-Curie grant agreement no. 956548 (QUANTIMONY) for financial support.

AUTHOR DECLARATIONS

Conflict of Interest

The authors have no conflicts to disclose.

Author Contributions

Takuma Sato: Conceptualization (equal): Software (lead); Data curation (lead); Formal analysis (equal); Methodology (equal); Visualization (lead); Writing - original draft (lead); Writing - review & editing (equal). Borislav Petrović: Conceptualization (equal); Data curation (supporting); Formal analysis (equal); Visualization (supporting); Writing - original draft (supporting); Writing - review & editing (equal). Robert Weih: Validation (equal); Writing - review & editing (equal). Fabian Hartmann: Validation (equal); Writing - review & editing (equal). **Sven Höfling**: Funding acquisition (equal); Validation (equal); Writing - review & editing (equal). Stefan Birner: Funding acquisition (equal); Project administration (lead); Resources (equal); Supervision (supporting). Christian Jirauschek: Resources (equal); Validation (supporting); Writing - review & editing (equal). Thomas Grange: Conceptualization (equal); Methodology (equal); Software (supporting); Supervision (lead); Validation (equal); Writing - review & editing (equal).

DATA AVAILABILITY

The data that support the findings of this study are openly available in Zenodo at https://doi.org/10.5281/zenodo.17642241.

- ¹J. R. Meyer, W. W. Bewley, C. L. Canedy, C. S. Kim, M. Kim, C. D. Merritt, and I. Vurgaftman, "The interband cascade laser," Photonics 7, 75 (2020).
- 2 C.-H. Lin, R. Q. Yang, D. Zhang, S. J. Murry, S. S. Pei, A. A. Allerman, and S. R. Kurtz, "Type-II interband quantum cascade laser at 3.8 μm ," Elect. Lett. **33**, 598 (1997).
- ³G. Wysocki, Y. Bakhirkin, S. So, F. K. Tittel, C. J. Hill, R. Q. Yang, and M. P. Fraser, "Dual interband cascade laser based trace-gas sensor for environmental monitoring," Appl. Opt. 46, 8202 (2007).
- ⁴M. von Edlinger, J. Scheuermann, R. Weih, L. Nähle, M. Fischer, J. Koeth, S. Höfling, and M. Kamp, "Interband cascade lasers for applications in process control and environmental monitoring," in *Light, Energy and the Environment 2015* (Optica, 2015) p. EM2A.5.
- ⁵B. Henderson, A. Khodabakhsh, M. Metsälä, I. Ventrillard, F. M. Schmidt, D. Romanini, G. A. D. Ritchie, S. te Lintel Hekkert, R. Briot, T. Risby, et al., "Laser spectroscopy for breath analysis: towards clinical implementation," Appl. Phys. B **124**, 161 (2018).
- ⁶A. Delga and L. Leviandier, "Free-space optical communications with quantum cascade lasers," in *Quantum sensing and nano electronics and photonics XVI*, Vol. 10926 (SPIE, 2019) p. 140.
- ⁷J. R. Meyer, C. A. Hoffman, F. J. Bartoli, and L. R. Ram-Mohan, "Type-II quantum-well lasers for the mid-wavelength infrared," Appl. Phys. Lett. **67**, 757 (1995).
- ⁸K. Ryczko, G. Sęk, and J. Misiewicz, "Eight-band k·p modeling of InAs/InGaAsSb type-II W-design quantum well structures for interband cascade lasers emitting in a broad range of mid infrared," J. Appl. Phys. **114**, 223519 (2013).
- ⁹F. Janiak, M. Motyka, G. Sęk, M. Dyksik, K. Ryczko, J. Misiewicz, R. Weih, S. Höfling, M. Kamp, and G. Patriarche, "Effect of arsenic on the optical properties of GaSb-based type II quantum wells with quaternary GaInAsSb layers," J. Appl. Phys. 114, 223510 (2013).

- ¹⁰M. Motyka, K. Ryczko, M. Dyksik, G. Sęk, J. Misiewicz, R. Weih, M. Dallner, S. Höfling, and M. Kamp, "On the modified active region design of interband cascade lasers," J. Appl. Phys. **117**, 084312 (2015).
- ¹¹M. Motyka, M. Dyksik, K. Ryczko, R. Weih, M. Dallner, S. Höfling, M. Kamp, G. Sęk, and J. Misiewicz, "Type-II quantum wells with tensile-strained GaAsSb layers for interband cascade lasers with tailored valence band mixing," Appl. Phys. Lett. 108, 101905 (2016).
- ¹²M. Dyksik, M. Motyka, M. Kurka, K. Ryczko, J. Misiewicz, A. Schade, M. Kamp, S. Höfling, and G. Sęk, "Electrical tuning of the oscillator strength in type II InAs/GaInSb quantum wells for active region of passively mode-locked interband cascade lasers," Jpn. J. Appl. Phys. 56, 110301 (2017).
- ¹³B. Petrović, T. Sato, S. Birner, J. Zanon, M. E. Flatté, R. Weih, F. Hartmann, and S. Höfling, "Triple V-shaped type-II quantum wells for long wavelength interband cascade lasers," Phys. Lett. A 561, 130971 (2025).
- ¹⁴H. Knötig, J. Nauschütz, N. Opačak, S. Höfling, J. Koeth, R. Weih, and B. Schwarz, "Mitigating valence intersubband absorption in interband cascade lasers," Laser & Photonics Rev. 16, 2200156 (2022).
- 15 J. Nauschütz, H. Knötig, R. Weih, J. Scheuermann, J. Koeth, S. Höfling, and B. Schwarz, "Pushing the room temperature continuous-wave operation limit of GaSb-based interband cascade lasers beyond 6 $\mu \rm m$," Laser & Photonics Rev. 17, 2200587 (2023).
- ¹⁶C. H. Grein, P. M. Young, M. E. Flatté, and H. Ehrenreich, "Long wavelength InAs/InGaSb infrared detectors: Optimization of carrier lifetimes," J. Appl. Phys. **78**, 7143 (1995).
- ¹⁷C. H. Grein, M. E. Flatté, J. T. Olesberg, S. A. Anson, L. Zhang, and T. F. Boggess, "Auger recombination in narrow-gap semiconductor superlattices incorporating antimony," J. Appl. Phys. 92, 7311 (2002).
- ¹⁸I. Vurgaftman, W. W. Bewley, C. L. Canedy, C. S. Kim, M. Kim, C. D. Merritt, J. Abell, J. R. Lindle, and J. R. Meyer, "Rebalancing of internally generated carriers for mid-infrared interband cascade lasers with very low power consumption," Nat. Comm. 2, 585 (2011).
- ¹⁹W. B. William, L. C. Chadwick, S. K. Chul, K. Mijin, D. M. Charles, A. Joshua, V. Igor, and R. M. Jerry, "High-power room-temperature continuous-wave mid-infrared interband cascade lasers," Opt. Express 20, 20894 (2012).
- ²⁰R. Weih, Interbandkaskadenlaser für die Gassensorik im Spektralbereich des mittleren Infrarot, Ph.D. dissertation, Julius-Maximilians-Universität Würzburg (2018).
- ²¹L. Olafsen, E. Aifer, I. Vurgaftman, W. Bewley, C. Felix, J. Meyer, D. Zhang, C.-H. Lin, and S. Pei, "Near-roomtemperature mid-infrared interband cascade laser," Appl. Phys. Lett. **72**, 2370 (1998).
- ²²A. Bauer, M. Dallner, M. Kamp, S. Höfling, L. Worschech, and A. Forchel, "Shortened injector interband cascade lasers for 3.3to 3.6-\(\mu\)m emission," Optical Engineering 49, 111117 (2010).
- ²³I. Vurgaftman, M. P. Lumb, and J. R. Meyer, Bands and Photons in III-V Semiconductor Quantum Structures (Oxford University Press, 2020).
- ²⁴F. Pilat, A. Windischhofer, M. Beiser, V. F. Pecile, E. Gangrskaia, A. Pugžlys, R. Weih, J. Koeth, A. Baltuška, O. H. Heckl, and B. Schwarz, "Fast gain dynamics in interband cascade lasers," Laser & Photonics Rev. 19, 2400867 (2025).
- ²⁵W. W. Chow and S. W. Koch, Semiconductor-Laser Fundamentals (Springer, 1999).
- ²⁶T. Grange, "Electron transport in quantum wire superlattices," Phys. Rev. B 89, 165310 (2014).
- ²⁷U. Aeberhard, "Quantum transport simulation of hot carrier photocurrent generation in quantum well solar cells," Semicond. Sci. Technol. 34, 094002 (2019).
- ²⁸ A. Kolek, "Interband tunneling in a type-II broken-gap superlattice," Phys. Rev. Appl. 19, 024059 (2023).

- ²⁹Y.-M. Mu and S. S. Pei, "Effects of anisotropic k-p interactions on energy bands and optical properties of type-II interband cascade lasers," J. Appl. Phys. **96**, 1866 (2004).
- ³⁰S.-C. Lee, F. Banit, M. Woerner, and A. Wacker, "Quantum mechanical wavepacket transport in quantum cascade laser structures," Phys. Rev. B 73, 245320 (2006).
- ³¹S. L. Chuang, *Physics of Optoelectronic Devices* (Wiley, New York, 1995).
- ³²J. S. Blakemore, Semiconductor statistics (Courier Corporation, 2002).
- ³³N. K. Dutta, "Calculation of Auger rates in a quantum well structure and its application to InGaAsP quantum well lasers," J. Appl. Phys. **54**, 1236 (1983).
- ³⁴W. W. Bewley, J. R. Lindle, C. S. Kim, M. Kim, C. L. Canedy, I. Vurgaftman, and J. R. Meyer, "Lifetimes and Auger coefficients in type-II W interband cascade lasers," Appl. Phys. Lett. 93, 041118 (2008).
- ³⁵J. R. Meyer, C. L. Canedy, M. Kim, C. S. Kim, C. D. Merritt, W. W. Bewley, and I. Vurgaftman, "Comparison of Auger coefficients in type I and type II quantum well midwave infrared lasers," IEEE J. Quantum Elect. 57, 2500110 (2021).
- ³⁶M. E. Flatté, C. H. Grein, T. C. Hasenberg, S. A. Anson, D.-J. Jang, J. T. Olesberg, and T. F. Boggess, "Carrier recombination rates in narrow-gap InAs/Ga_{1-x}In_xSb-based superlattices," Phys. Rev. B **59**, 5745 (1999).
- ³⁷ J. Hader, J. V. Moloney, and S. W. Koch, "Microscopic evaluation of spontaneous emission- and Auger-processes in semiconductor lasers," IEEE J. Quantum Elect. 41, 1217 (2005).
- ³⁸J. Hader, J. V. Moloney, and S. W. Koch, "Supression of carrier recombination in semiconductor lasers by phase-space filling," Appl. Phys. Lett. 87, 201112 (2005).
- ³⁹U. Bockelmann and T. Egeler, "Electron relaxation in quantum dots by means of Auger processes," Phys. Rev. B 46, 15574 (1992).
- 40 O. Gilard, F. Lozes-Dupuy, G. Vassilieff, J. Barrau, and P. Le Jeune, "Theoretical study of Auger effect in 1.5 μm quantum-well lasers," J. Appl. Phys. **84**, 2705 (1998).
- ⁴¹B. V. Olson, C. H. Grein, J. K. Kim, E. A. Kadlec, J. F. Klem, S. D. Hawkins, and E. A. Shaner, "Auger recombination in longwave infrared InAs/InAsSb type-II superlattices," Appl. Phys. Lett. 107, 261104 (2015).
- ⁴²H. Knötig, Interband cascade lasers and detectors: From active region design to devices, Ph.D. thesis, Technische Universität Wien (2022).
- ⁴³L. Cerutti, D. A. D. Thomas, J.-B. Rodriguez, M. R. Calvo, G. Patriarche, A. N. Baranov, and E. Tournié, "Quantum well interband semiconductor lasers highly tolerant to dislocations," Optica 8, 1397 (2021).
- ⁴⁴M. Fagot, D. A. Díaz-Thomas, A. Gilbert, M. Ramonda, Y. Rouillard, J.-B. Rodriguez, E. Tournié, and L. Cerutti, "Highperformance GaSb-based interband cascade lasers emitting at 4.7 μm grown on GaAs and Si substrates," Opt. Mater. Express 15, 2654 (2025).
- ⁴⁵W. P. Dumke, "Quantum theory of free carrier absorption," Phys. Rev. **124**, 1813 (1961).
- ⁴⁶A. Windischhofer, N. Opačak, and B. Schwarz, "Charge Transport in Interband Cascade Lasers: An Ab-Initio Self-Consistent Model," Laser Photonics Rev. 19, 2400866 (2024).
- ⁴⁷W. W. Bewley, J. R. Lindle, C. L. Canedy, M. Kim, C. S. Kim, D. C. Larrabee, I. Vurgaftman, and J. R. Meyer, "Gain, loss, and internal efficiency in interband cascade lasers emitting at $\lambda = 3.6$ –4.1 μm," J. Appl. Phys. **103**, 013114 (2008).
- ⁴⁸B. A. Foreman, "Elimination of spurious solutions from eightband k·p theory," Phys. Rev. B 56, R12748 (1997).
- ⁴⁹P. Y. Yu and M. Cardona, Fundamentals of Semiconductors, 3rd ed. (Springer, 2001).
- ⁵⁰S. Birner, Modeling of semiconductor nanostructures and semiconductor-electrolyte interfaces, Ph.D. dissertation, Walter Schottky Institut, Technische Universität München (2011).

- ⁵¹T. B. Bahder, "Eight-band k·p model of strained zinc-blende crystals," Phys. Rev. B 41, 11992 (1990).
- ⁵²X. Cartoixa, Theoretical Methods for Spintronics in Semiconductors with Applications, Ph.D. dissertation, California Institute of Technology (2002).
- ⁵³P. Lawaetz, "Valence-band parameters in cubic semiconductors," Phys. Rev. B 4, 3460 (1971).
- ⁵⁴D. Bimberg, R. Blachnik, M. Cardona, P. J. Dean, T. Grave, G. Harbeke, K. Hübner, U. Kaufmann, W. Kress, O. Madelung, W. von Münch, U. Rössler, J. Schneider, M. Schulz, and M. S. Skolnick, Landolt-Bornstein: Numerical Data and Functional Relationships in Science and Technology. New Series, edited by O. Madelung, Vol. III/17a (Springer-Verlag, 1982).
- ⁵⁵S. Hackenbuchner, Elektronische Struktur von Halbleiter-Nanobauelementen im thermodynamischen Nichtgleichgewicht, Ph.D. dissertation, Walter Schottky Institut, Technische Universität München (2002).
- ⁵⁶W. R. Frensley and R. N. Mir, "Simple remedy for spurious states in discrete k·p models of semiconductor structures," arXiv 1412.7201 (2015).
- ⁵⁷B. Petrović, A. Bader, J. Nauschütz, T. Sato, S. Birner, R. Weih, F. Hartmann, and S. Höfling, "Comparison between InAs-based and GaSb-based interband cascade lasers with hybrid superlattice plasmon-enhanced claddings," Opt. Mater. Express 14, 2912 (2024).
- ⁵⁸H. A. Bethe and E. E. Salpeter, Quantum Mechanics of Oneand Two-Electron Atoms (Springer, 1957).
- ⁵⁹R. Mac, D. Ban, and E. Dupont, "First-order k · p methods for electron intersubband scatterings in quantum wells," Phys. Rev. B 110, 165304 (2024).
- ⁶⁰R. Karplus and J. M. Luttinger, "Hall effect in ferromagnetics," Phys. Rev. **95**, 1154 (1954).
- ⁶¹F. Szmulowicz, "Derivation of a general expression for the momentum matrix elements within the envelope-function approximation," Phys. Rev. B **51**, 1613 (1995).
- ⁶²L. Hedin, "New method for calculating the one-particle Green's function with application to the electron-gas problem," Phys. Rev. 139, A796 (1965).
- ⁶³G. Stefanucci and R. van Leeuwen, Nonequilibrium Many-Body Theory of Quantum Systems, 2nd ed. (Cambridge University Press, 2025).
- ⁶⁴K. S. Thygesen and A. Rubio, "Conserving GW scheme for nonequilibrium quantum transport in molecular contacts," Phys. Rev. B **77**, 115333 (2008).
- ⁶⁵T. Kubis, C. Yeh, P. Vogl, A. Benz, G. Fasching, and C. Deutsch, "Theory of nonequilibrium quantum transport and energy dissipation in terahertz quantum cascade lasers," Phys. Rev. B 79,

- 195323 (2009).
- ⁶⁶D. O. Winge, M. Franckié, C. Verdozzi, A. Wacker, and M. F. Pereira, "Simple electron-electron scattering in non-equilibrium Green's function simulations," J. Phys.: Conference Series 696, 012013 (2016).
- ⁶⁷L. Deuschle, J. Backman, M. Luisier, and J. Cao, "Ab initio self-consistent GW calculations in non-equilibrium devices: Auger recombination and electron-electron scattering," in *International Conference on Simulation of Semiconductor Processes and Devices (SISPAD)* (2023) p. 297.
- ⁶⁸G. Montoya, J. Alberto, T. Alberto, G. Michele, and B. Francesco, "Nonequilibrium Green's function study of phonondressed Auger transitions in superlattice infrared photodetectors," Phys. Rev. Appl. 23, 014050 (2025).
- ⁶⁹R. Binder and S. W. Koch, "Nonequilibrium semiconductor dynamics," Prog. Quantum Electron. 19, 307 (1995).
- ⁷⁰H. Haug and S. W. Koch, Quantum Theory of the Optical and Electronic Properties of Semiconductors, 5th ed. (WORLD SCI-ENTIFIC, 2009).
- ⁷¹M. Makowiec and A. Kolek, "Machine-learning-enhanced NEGF solver of interband cascade laser," in *International Conference on Numerical Simulation of Optoelectronic Devices (NUSOD)* (IEEE, 2024) p. 23.

Appendix A: 8-band $\mathbf{k} \cdot \mathbf{p}$ Hamiltonian

We find the energy eigenstates in a heterostructure of zincblende crystals within the envelope function approximation. Each material layer is described by the following 8-band $\mathbf{k} \cdot \mathbf{p}$ Hamiltonian,

$$\boldsymbol{H}_0(\mathbf{k},\varepsilon) = \boldsymbol{H}_{\mathrm{kp}}^{8\times8} + \boldsymbol{H}_{\Delta}^{8\times8} + \boldsymbol{H}_{\varepsilon}^{8\times8},$$
 (A1)

in the basis $\{|S\uparrow\rangle, |X\uparrow\rangle, |Y\uparrow\rangle, |Z\uparrow\rangle, |S\downarrow\rangle, |X\downarrow\rangle, |Y\downarrow\rangle, |Z\downarrow\rangle\}$. The $\mathbf{k} \cdot \mathbf{p}$ Hamiltonian,

$$\boldsymbol{H}_{\mathrm{kp}}^{8\times8} = \begin{pmatrix} H_{\mathrm{cc}} & \boldsymbol{H}_{\mathrm{cv}} \\ \boldsymbol{H}_{\mathrm{vc}} & \boldsymbol{H}_{\mathrm{vv}} \\ & H_{\mathrm{cc}} & \boldsymbol{H}_{\mathrm{cv}} \\ & \boldsymbol{H}_{\mathrm{vc}} & \boldsymbol{H}_{\mathrm{vv}} \end{pmatrix}, \quad (A2)$$

contains the free kinetic energy $\hbar^2 k^2/(2m_0)$, $\mathbf{k} \cdot \mathbf{p}$ interband coupling $\mathcal{O}(k)$, and the lowest order $\mathbf{k} \cdot \mathbf{p}$ coupling via remote bands $\mathcal{O}(k^2)$:

$$H_{\rm cc} = E_{\rm c}(T_{\rm L}) + \frac{\hbar^2}{2m_0} \left(k_x S k_x + k_y S k_y + k_z S k_z \right), \tag{A3a}$$

$$\mathbf{H}_{cv} = \left(iPk_x + k_y \frac{B}{2}k_z + k_z \frac{B}{2}k_y \ iPk_y + k_z \frac{B}{2}k_x + k_x \frac{B}{2}k_z \ iPk_z + k_x \frac{B}{2}k_y + k_y \frac{B}{2}k_x\right), \tag{A3b}$$

$$\mathbf{H}_{vc} = \left(-ik_{x}P + k_{z}\frac{B}{2}k_{y} + k_{y}\frac{B}{2}k_{z} - ik_{y}P + k_{x}\frac{B}{2}k_{z} + k_{z}\frac{B}{2}k_{x} - ik_{z}P + k_{y}\frac{B}{2}k_{x} + k_{x}\frac{B}{2}k_{y}\right)^{t},$$
(A3c)

$$\boldsymbol{H}_{\mathrm{vv}} = \left(E_{\mathrm{v,av}} + \frac{\hbar^2 k^2}{2m_0}\right) \boldsymbol{I}_3$$

$$+\begin{pmatrix} k_{x}L'k_{x}+k_{y}Mk_{y}+k_{z}Mk_{z} & k_{x}N^{+'}k_{y}+k_{y}N^{-'}k_{x} & k_{x}N^{+'}k_{z}+k_{z}N^{-'}k_{x} \\ k_{y}N^{+'}k_{x}+k_{x}N^{-'}k_{y} & k_{x}Mk_{x}+k_{y}L'k_{y}+k_{z}Mk_{z} & k_{y}N^{+'}k_{z}+k_{z}N^{-'}k_{y} \\ k_{z}N^{+'}k_{x}+k_{x}N^{-'}k_{z} & k_{z}N^{+'}k_{y}+k_{y}N^{-'}k_{z} & k_{x}Mk_{x}+k_{y}Mk_{y}+k_{z}L'k_{z} \end{pmatrix},$$
(A3d)

where m_0 is the bare electron mass. $E_{v,av}$ is the average of the heavy-hole, light-hole and spin-orbit split-off band

offsets of bulk in the absence of strain. The conduction

band offset is calculated from the valence band offset, spin-orbit splitting energy $\Delta_{\rm so}$, 0 K band gap, and the Varshni shift as

$$E_{\rm c}(T_{\rm L}) = E_{\rm v,av} + \Delta_{\rm so}/3 + E_{\rm g}(T_{\rm L}),$$
 (A4)

$$E_{\rm g}(T_{\rm L}) = E_{\rm g}(0) - \frac{\alpha T_{\rm L}^2}{T_{\rm L} + \beta}.$$
 (A5)

The dimensionless parameter S contains the kinetic energy of free electron and remote-band contributions,

$$S = 1 + \frac{2}{m_0} \sum_{r \in \text{remote}} \frac{|\langle S\sigma|\hat{p}_x|r\sigma\rangle|^2}{E_c(0) - E_r}, \quad (A6)$$

which is independent of the spin $\sigma = \uparrow, \downarrow$. The parameter $P = (i\hbar/m_0)\langle S\sigma|\hat{p}_x|X\sigma\rangle = (i\hbar/m_0)\langle S\sigma|\hat{p}_y|Y\sigma\rangle = (i\hbar/m_0)\langle S\sigma|\hat{p}_z|Z\sigma\rangle = \hbar\sqrt{E_P/(2m_0)}$ couples the conduction and valence band states and is calculated from the Kane energy E_P . The asymmetric ordering of the linear-k terms is to guarantee that integration of the envelope-function Schrödinger equation across material interfaces yields the correct number of boundary conditions in the limit $S \to 0$. This limit avoids spurious solutions originating from the highest-order k-term of the secular equation. 23,48 In order not to damage the band structure, we adjust E_P to preserve the conduction band effective mass of each layer,

$$\frac{m_0}{m_{\rm e}(T_{\rm L})} = S + \frac{E_{\rm P}}{3} \left[\frac{2}{E_{\rm g}(T_{\rm L})} + \frac{1}{E_{\rm g}(T_{\rm L}) + \Delta_{\rm so}} \right],$$
 (A7)

when setting S to 0. B is an additional interband coupling via remote bands and causes spin-splitting in crystals without bulk inversion symmetry.⁴⁹ Unlike the P terms, we symmetrize the B terms so that the bulk Hamiltonian is invariant under a 90° rotation around x, y, and z crystal axes. L', M, and

$$N^{\pm'} = \frac{N'}{2} \mp \frac{\hbar^2}{2m_0} (3\kappa' + 1),$$
 (A8)

are the valence-band equivalent of the S parameter and have the dimension of $\hbar^2/(2m_0)$. L', N', and κ' are shifted from their 6-band counterparts since the contribution of the conduction band, which is treated exactly and not as a remote band in the 8-band model, must be subtracted off.⁵⁰

$$L' \equiv L_6 + \frac{P^2}{E_{\rm g}(0)},$$
 (A9a)

$$N' = N_6 + \frac{P^2}{E_g(0)},$$
 (A9b)

$$\kappa' = \kappa_6 - \frac{1}{6} \frac{E_{\rm P}}{E_{\rm g}(0)},\tag{A9c}$$

where the band gap is without the Varshni shift since the 6- and 8-band $\mathbf{k} \cdot \mathbf{p}$ theories are constructed at 0 K. The 6-band Dresselhaus–Kip–Kittel parameters are calculated from the Luttinger parameters as⁵¹

$$L_6 = -\frac{\hbar^2}{2m_0} \left(\gamma_1 + 4\gamma_2 + 1 \right),$$
 (A10a)

$$M = -\frac{\hbar^2}{2m_0} (\gamma_1 - 2\gamma_2 + 1),$$
 (A10b)

$$N_6 = -\frac{\hbar^2}{2m_0} 6\gamma_3. (A10c)$$

The spin-orbit splitting of the valence band states is

$$\boldsymbol{H}_{\Delta}^{8\times8} = \begin{pmatrix} \boldsymbol{H}_{\Delta\uparrow\uparrow} & \boldsymbol{H}_{\Delta\uparrow\downarrow} \\ \boldsymbol{H}_{\Delta\uparrow\downarrow}^{\dagger} & \boldsymbol{H}_{\Delta\uparrow\uparrow}^{*} \end{pmatrix}, \tag{A11}$$

where

$$\mathbf{H}_{\Delta\uparrow\uparrow} = \frac{\Delta_{\text{so}}}{3} \begin{pmatrix} 0 & 0 & 0 & 0 \\ 0 & 0 & -\mathbf{i} & 0 \\ 0 & \mathbf{i} & 0 & 0 \\ 0 & 0 & 0 & 0 \end{pmatrix},$$
(A12a)

$$\mathbf{H}_{\Delta\uparrow\downarrow} = \frac{\Delta_{\text{so}}}{3} \begin{pmatrix} 0 & 0 & 0 & 0 \\ 0 & 0 & 0 & 1 \\ 0 & 0 & 0 & -\mathrm{i} \\ 0 & -1 & \mathrm{i} & 0 \end{pmatrix}.$$
 (A12b)

The elastic deformation energy is considered to first order in the strain tensor field $\varepsilon(z)$.

$$\boldsymbol{H}_{\varepsilon}^{8\times8} = \begin{pmatrix} D_{\mathrm{c}}(\varepsilon) & & \\ & \boldsymbol{D}_{\mathrm{v}}(\varepsilon) & \\ & & D_{\mathrm{c}}(\varepsilon) & \\ & & \boldsymbol{D}_{\mathrm{v}}(\varepsilon) \end{pmatrix}, \quad (A13)$$

where

Symbol	InAs	AlSb	GaSb	InSb	units	Ref.
\overline{a}	0.60583	0.61355	0.60959	0.64794	nm	23
C_{11}	83.29	87.69	88.42	68.47	GPa	23
C_{12}	45.26	43.41	40.26	37.35	GPa	23
C_{44}	39.59	40.76	43.22	31.11	GPa	23
$E_{ m v,av}$	-0.7423	-0.6353	-0.2833	-0.27	${ m eV}$	23
$E_{ m g}$	0.417	2.386	0.812	0.235	${ m eV}$	23
α	3.07×10^{-4}	4.2×10^{-4}	4.17×10^{-4}	3.20×10^{-4}	eV/K	23
β	191	140	140	170	K	23
S	-1	-0.12	-1	0.54	-	23
$E_{ m P}$	19.5	18.7	25.8	23.3	${ m eV}$	23
B	3.596	0	13.079	2.703	${ m eV}$	52
γ_1	19.7	5.18	13.4	34.8	-	23
γ_2	8.4	1.19	4.7	15.5	-	23
γ_3	9.3	1.97	6	16.5	-	23
κ	7.68	0.31	3.18	14.76	-	53
$\Delta_{ m so}$	0.367	0.676	0.76	0.81	${ m eV}$	23
Ξ	-5.08	-4.5	-7.5	-6.94	${ m eV}$	23
$a_{ m v}$	1	1.4	0.8	0.36	${ m eV}$	23
b	-1.8	-1.35	-2	-2	${ m eV}$	23
d	-3.6	-4.3	-4.7	-4.7	${ m eV}$	23
$\epsilon(0)$	15.15	12.04	15.69	17.5	-	54

TABLE II. Material parameters used in the simulations.

TABLE III. Ternary bowing parameters used in the simulations.

Parameter	$Ga_{1-x}In_xSb$	units	Ref.
$E_{\rm v,av}$	-0.033	eV	23
$E_{ m v,av} \ E_{ m g}$	0.415	${ m eV}$	23
α	0	$\mathrm{eV/K}$	23
β	0	K	23
S	0	_	23
$E_{ m P}$	7.8	${ m eV}$	23
$\Delta_{ m so}$	0.1	${ m eV}$	23

$$D_{c}(\varepsilon) = \Xi(\varepsilon_{11} + \varepsilon_{22} + \varepsilon_{33}), \tag{A14a}$$

$$\mathbf{D}_{\mathbf{v}}(\varepsilon) = \begin{pmatrix} l_{\varepsilon}\varepsilon_{11} + m_{\varepsilon}(\varepsilon_{22} + \varepsilon_{33}) & n_{\varepsilon}\varepsilon_{12} & n_{\varepsilon}\varepsilon_{13} \\ n_{\varepsilon}\varepsilon_{12} & l_{\varepsilon}\varepsilon_{22} + m_{\varepsilon}(\varepsilon_{11} + \varepsilon_{33}) & n_{\varepsilon}\varepsilon_{23} \\ n_{\varepsilon}\varepsilon_{13} & n_{\varepsilon}\varepsilon_{23} & l_{\varepsilon}\varepsilon_{33} + m_{\varepsilon}(\varepsilon_{11} + \varepsilon_{22}) \end{pmatrix}.$$
(A14b)

 $\varepsilon(z)$ is calculated for each heterostructure layer from its lattice constant a and the elastic stiffness constants C_{ij} assuming pseudomorphic growth on a GaSb substrate. The conduction band is only sensitive to hydrostatic strains (coefficient Ξ) as the band has spherical symmetry. The coefficients in the valence band consist of the hydrostatic, uniaxial, and shear deformation potentials $(a_{\rm v},b,d)$: $l_{\varepsilon}=a_{\rm v}+2b,m_{\varepsilon}=a_{\rm v}-b,$ and $n_{\varepsilon}=\sqrt{3}d.$ All the material parameters are listed in Tables II and III.

The heterostructure Hamiltonian is a stack of the Hamiltonian A1 with k_z replaced with the differential operators due to translational asymmetry along the growth

direction,

$$\boldsymbol{H} = \boldsymbol{H}^{(0)} + \boldsymbol{H}^{(L)} \frac{\mathrm{d}}{\mathrm{d}z} + \frac{\mathrm{d}}{\mathrm{d}z} \boldsymbol{H}^{(R)} + \frac{\mathrm{d}}{\mathrm{d}z} \boldsymbol{H}^{(2)} \frac{\mathrm{d}}{\mathrm{d}z}, \text{ (A15)}$$

where $\mathbf{H}^{(0)}, \mathbf{H}^{(L)}, \mathbf{H}^{(R)}$, and $\mathbf{H}^{(2)}$ are 8×8 matrices dependent on position. The 8-band Hamiltonian is discretized on a real-space numerical grid by the finite difference method. We denote the resulting matrix by $\mathbf{H}^{8N \times 8N}$. Our $\mathbf{k} \cdot \mathbf{p}$ solver is resistant to spurious solutions by virtue of the rescaling of S described above and a consistent discretization of the differential operators. The first derivatives in Eq. (A15) are discretized with

TABLE IV.	Geometry and numerical parameters used in the
simulations.	

Symbol	value	units
$T_{ m L}$	300	K
$T_{ m e}$	300	K
$E_{\rm cutoff}^{\rm c}$	1000	meV
$E_{ m cutoff}^{ m v}$	500	meV
$E_{ m cutoff}^{ m c} \ E_{ m cutoff}^{ m l} \ E_{ m cutoff}^{ m \parallel}$	300	meV
$\gamma_{ m subband}$	15	meV
$\gamma_{ m gain}$	20	meV
\hat{e}	(0.998, 0, 0.059)	-
$L_{\rm cav}$	2	$\mu\mathrm{m}$
R	0.31	-
Γ	0.217	-
$\alpha_{ m clad}$	2.08	cm^{-1}
$\lambda_{ m s}$	4	nm

forward and backward rather than centered differences to avoid oscillatory solutions.^{55,56} The hermiticity of the resulting matrix and the consistency in the allocation of material parameters⁵⁶ restrict the choice of discretization schemes for the differential operators in Eq. (A15).

Appendix B: Simulation parameters

Table IV summarizes the geometry and numerical parameters used in this study. The mirror reflectivity R was derived from the average refractive index $n_{\rm r} \approx 3.5$ of the active region. The optical confinement factor Γ was calculated by a Helmholtz equation solver. The cladding loss was obtained by the Drude model and a mobility model that depends on the carrier concentration.⁵⁷

Appendix C: Oscillator strengths

While the envelope function overlap represents a major part of the oscillator strength of ICL lasing levels, the net material gain also involves intraband transitions. Therefore, the envelope overlap alone is not sufficient to evaluate the net gain. Calculation of the oscillator strengths requires a matrix representation of the dipole operator along the z axis and the momentum operator in the x-y plane. The energy eigenstates of \mathbf{H}_{RRS} are used as the basis for a better compatibility with the NEGF formalism. The z component is readily obtained by rotating the diagonal matrix $\operatorname{diag}(z_1, z_2, \cdots)$.

For the in-plane directions $j \in \{x,y\}$, we opt for the momentum picture of the light-carrier interaction since the position operator \hat{x}_j in the directions of translational invariance is ambiguous. The oscillator strengths calculated from the momentum and dipole pictures are equal if (i) the momentum operator coincides with the commutator $(m_0/i\hbar)[\hat{x}_j,\hat{H}]$, and (ii) the oscillator strength is represented in the eigenbasis of \hat{H} . The requirement

(i) is not straightforward when the Hamiltonian contains spin-orbit coupling, second-order $\mathbf{k} \cdot \mathbf{p}$ coupling via remote bands⁵⁹ as in Eq. (A6), or position-dependent parameters. Nevertheless, we retain consistency with the growth direction by defining the in-plane momentum operator by $\hat{p}_j \equiv (m_0/i\hbar)[\hat{x}_j, \hat{H}]$. For homogeneous infinite lattices, the $\mathbf{k} \cdot \mathbf{p}$ perturbation theory^{60,61} shows that

$$\frac{m_0}{\mathrm{i}\hbar} \left[\hat{x}_j, \hat{H}_{\mathrm{kp}}(\mathbf{k}) \right]_{\nu\nu'} = \frac{m_0}{\hbar} \left[\frac{\partial \hat{H}_{\mathrm{kp}}(\mathbf{k})}{\partial k_j} \right]_{\nu\nu'} + \mathcal{O}(k^2), \text{ (C1)}$$

where ν and ν' enumerate the $\mathbf{k} \cdot \mathbf{p}$ bands considered in the model. We neglect the second and higher order terms according to the accuracy of the Hamiltonian (A1). For heterostructures, it is tempting to assign Eq. (C1) to each real-space grid points with position-dependent material parameters. However, the confinement along the growth direction (derivatives $\mathrm{d}/\mathrm{d}z$) affects $\hat{p}_{x,y}$ via the products $k_x k_z$ and $k_y k_z$ in the Hamiltonian (A3d). We instead insert the heterostructure Hamiltonian [Eq. (A15)] after discretization into Eq. (C1) to obtain the matrix representation in the tensor product basis of the $\mathbf{k} \cdot \mathbf{p}$ bands and real-space coordinates (enumerated by s, s'),

$$(\hat{p}_j)_{ss'} = \frac{m_0}{\hbar} \frac{\partial \boldsymbol{H}_{ss'}^{8N \times 8N}(\mathbf{k}_{\parallel})}{\partial k_i}.$$
 (C2)

The matrix is transformed first to the RRS basis and then to the eigenbasis of $\boldsymbol{H}_{\text{RRS}}$, and is substituted to Fermi's golden rule.

Quantum confinement and selection rules at each \mathbf{k}_{\parallel} point are encoded in these matrix elements. An optimally designed W-QW is asymmetrical and the oscillator strength between the lasing levels reaches the maximum approximately at the threshold electric field. However, the relative increase in an asymmetric W-QW design is much milder than e.g. for triple electron well designs. ^{12,13} We thus neglect the bias-dependence in Eq. (C2).

Consequently, the oscillator strength between two energy eigenstates at the in-plane momentum ${\bf k}_{\parallel}$ is given by

$$O_{nm}(\hat{e}, \mathbf{k}_{\parallel}) = \frac{\hbar}{m_0^2 \omega_{nm}} \sum_{j=x,y} \left| e_j \langle n | \hat{p}_j(\mathbf{k}_{\parallel}) | m \rangle \right|^2 + \hbar \omega_{nm} \left| e_z \langle n | \hat{z} | m \rangle \right|^2,$$
 (C3)

where $\hbar\omega_{nm}$ is the energy separation of the two states.

Appendix D: Carrier-carrier scattering

The Auger process is an inelastic carrier-carrier scattering and therefore requires an approach beyond the Hartree–Fock approximation. Hedin⁶² proposed a perturbation expansion of Green's functions around the screened Coulomb interaction \boldsymbol{W} . Since \boldsymbol{W} describes the effective (dressed) interaction, approximations based

on this expansion are expected to describe the electronelectron interaction in a physically transparent manner. The screened Coulomb interaction defined on the Keldysh contour obeys Dyson's equation, ⁶³

$$W_{z_1 z_2}(1;2) = V_{z_1 z_2}(1;2) + \sum_{z_3 z_4} \int d3 \int d4 \ V_{z_1 z_3}(1;3) \Pi_{z_3 z_4}(3;4) W_{z_4 z_2}(4;2), \tag{D1}$$

where $1 = (x_1, y_1, t_1)$ is the spacetime coordinates of an electron and the indices z_i label the RRS modes. The bare Coulomb interaction is instantaneous, i.e., $V(1;2) \propto \delta(t_1 - t_2)$. Note that V and W have two instead of four mode indices as the RRS basis diagonalizes the position operator.^{26,64} The polarization function Π describes the excitation of the "partner" electron that interacts with the electron of interest.

The screened Coulomb interaction affects the electron of interest via the self-energy Σ . It consists of diagrams involving the Green's function and W. The GW approximation is to approximate Σ and Π in Eq. (D1) by the

lowest-order diagrams⁶³

$$\Sigma_{z_1 z_2}(1;2) \approx iG_{z_1 z_2}(1;2)W_{z_1 z_2}(1;2),$$
 (D2)

$$\Pi_{z_1 z_2}(1;2) \approx -G_{z_1 z_2}(1;2)G_{z_2 z_1}(2;1),$$
 (D3)

which account for inelastic carrier-carrier scattering. It has been used to improve the accuracy of current-voltage characteristics of THz quantum cascade lasers^{65,66} and recently to calculate Auger recombination in carbon nanotubes,⁶⁷ QW solar cells²⁷ and type-II superlattices.⁶⁸

The greater (>) component of Eq. (D1) is calculated assuming translational symmetry in the in-plane directions and steady states,

$$W_{\mathbf{q}_{\parallel}}^{>}(E) = W_{\mathbf{q}_{\parallel}}^{\mathrm{R}}(E)\Pi_{\mathbf{q}_{\parallel}}^{>}(E)W_{\mathbf{q}_{\parallel}}^{\mathrm{A}}(E).$$
 (D4)

The retarded (R) component of Eq. (D1) is calculated considering a three-dimensional interacting electron gas in a medium with the static dielectric constant $\epsilon_0 \epsilon(0)$. The matrices reduce to scalar functions in this case and

$$W_{\mathbf{q}}^{R}(t_{1};t_{2}) = V_{\mathbf{q}}^{R}(t_{1};t_{2}) + \int dt_{3} \int dt_{4} V_{\mathbf{q}}^{R}(t_{1};t_{3}) \Pi_{\mathbf{q}}^{R}(t_{3};t_{4}) W_{\mathbf{q}}^{R}(t_{4};t_{2}),$$
(D5)

where $V_{\bf q}^{\rm R}(t_1;t_2)=\delta(t_1-t_2)e^2/(\epsilon_0\epsilon(0)L^3q^2)$ is the bare Coulomb potential in the reciprocal space with the normalization volume L^3 . We further make the quasi-static screening approximation, i.e., assume that the electron gas is not too dense so that carriers rearrange themselves in response to an addition of an electron much faster than getting scattered by the environment. 69 $W_{\bf q}^{\rm R}$ becomes instantaneous and Eq. (D5) can be solved algebraically,

$$W_{\mathbf{q}}^{\mathbf{R}} = \frac{V_{\mathbf{q}}^{\mathbf{R}}}{1 - V_{\mathbf{q}}^{\mathbf{R}} \Pi_{\mathbf{q}}^{\mathbf{R}}}.$$
 (D6)

This can be seen as a renormalized Coulomb interaction with the effective screening length

$$\lambda_{\rm s}(\mathbf{q}) = \left(-q^2 V_{\mathbf{q}}^{\rm R} \Pi_{\mathbf{q}}^{\rm R}\right)^{-1/2}.\tag{D7}$$

Similarly to Eqs. (11) and (12), we approximate $\Pi_{\bf q}^{\rm R} \approx$

 $\Pi_0^{\rm R}$. To apply the resulting interaction,

$$W_{\mathbf{q}}^{\mathrm{R}} = \frac{V_{\mathbf{q}}^{\mathrm{R}}}{1 + (q\lambda_{\mathrm{s}})^{-2}} = \frac{e^2}{\epsilon_0 \epsilon(0) L^3} \frac{1}{q^2 + \lambda_{\mathrm{s}}^{-2}},$$
 (D8)

to QWs, we Fourier-transform q_z to z and obtain

$$W_{\mathbf{q}_{\parallel}}^{\mathbf{R}}(z) = \frac{e^2}{2\epsilon_0 \epsilon(0) L^2} \frac{e^{-q_{\mathrm{s}}|z|}}{q_{\mathrm{s}}}, \quad (D9a)$$

$$W_{\mathbf{q}_{\parallel}}^{\mathbf{A}} = \left(W_{\mathbf{q}_{\parallel}}^{\mathbf{R}}\right)^{\dagger} = W_{\mathbf{q}_{\parallel}}^{\mathbf{R}},$$
 (D9b)

where
$$q_{\rm s} = \sqrt{q_{\parallel}^2 + \lambda_{\rm s}^{-2}}$$
.

The evaluation of the screening length in Eq. (D7) is involved in general because the retarded polarization has a complex dependence on the subband occupation. As a first estimate, we deduce the retarded polarization by comparing the denominator of Eq. (D6) with the long-wavelength, static, and quasi-equilibrium limit of the

Lindhard dielectric function. 69,70 The carrier temperature is set to 300 K as in the gain calculation. The resulting screening length ranges from 1.8 nm to 3.0 nm for the designs in Table I and is of the same order of magnitude as the value used in this work, $\lambda_{\rm s}=4.0$ nm.

The Lindhard function in the static limit includes the

Debye–Hückel and Thomas–Fermi screening models as the non-degenerate (Maxwell–Boltzmann) and degenerate limiting cases, respectively. While the Debye screening length can be used in type-II superlattice photodetectors, ICL simulations may be more accurate with the Thomas–Fermi screening.⁷¹